Microstructural Hardening Mechanisms and Electrical Property Manipulations of Substantially Undercooled $Fe_{87}Cu_{13}$ Alloy

YUHAO WU, BAORONG ZHU, ZHENCHAO XIA, DAWEI YI, and JINGWEN SU

The microstructural hardening mechanisms and electrical property manipulations of undercooled $Fe_{87}Cu_{13}$ alloy have been investigated by systematical characterizations of Vickers microhardness and electrical impedance for glass-fluxed samples. Liquid $Fe_{87}Cu_{13}$ alloy was highly undercooled up to 399 K ($0.23\ T_L$). In small undercooling regime below 244 K, peritectic solidification happened, and a rise in undercooling contributed to the enhancement of primary dendrite growth velocity and copper content in dendrites and the refinement of solidification microstructures as well as the increase of both microhardness and impedance. When the rising undercooling attained 244 K, metastable phase separation occurred, and a Cu-rich shell was formed accompanied by a sudden drop of copper content in primary dendrites, microhardness and impedance. With a further improvement in undercooling, growth velocity of primary dendrites gradually increased and approached 22.0 m/s at the maximum undercooling. Meanwhile, dendrites contained more copper elements owing to the remarkable solute trapping effect, and the microhardness and impedance showed an upward trend. Numerical simulations revealed that surface segregation mainly dominated the liquid phase separation process if the copper proportion in Fe–Cu alloy was very low. Theoretical analyses demonstrated that the microhardness was closely related to the grain size, solute content and solidification velocity of primary phase whereas the magnitude of impedance was strongly dependent on the number of grain boundaries, crystal defects and vacancies.

YUHAO WU, BAORONG ZHU, DAWEI YI, and JINGWEN SU are with the College of Materials Science and Engineering, Xi'an University of Science and Technology, Xi'an 710054, P.R. China. Contact e-mail: yhwu@xust.edu.cn. ZHENCHAO XIA is with the School of Materials Engineering, Xi'an Aeronautical University, Xi'an 710077, P.R. China.
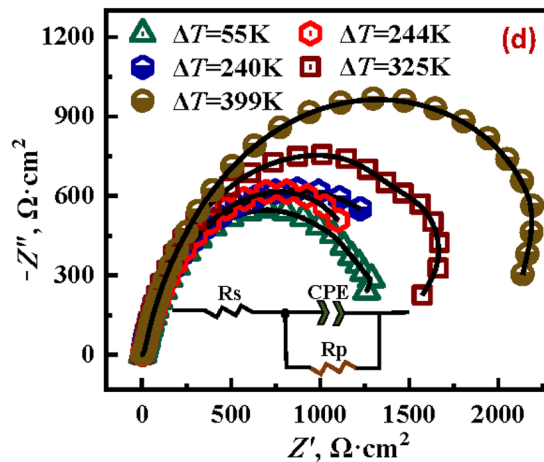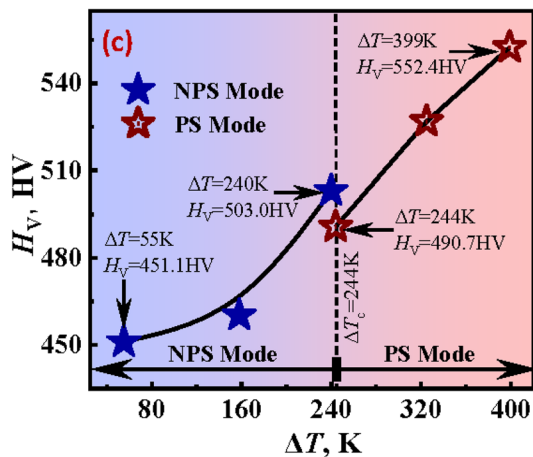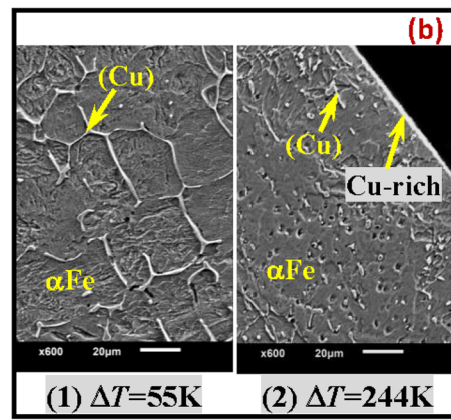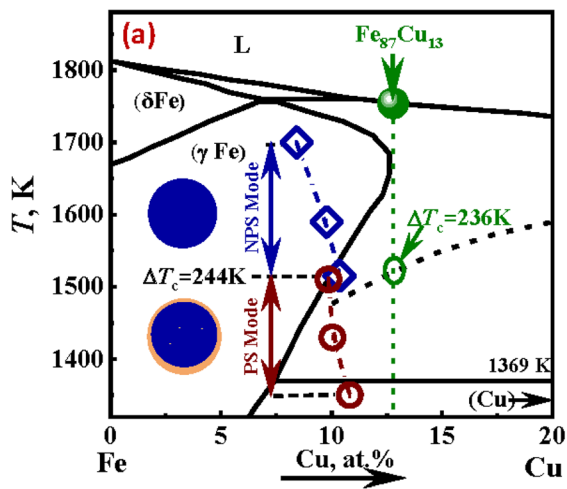
I. INTRODUCTION

OWING to the excellent characteristics of heat transfer and electric conduction for pure Fe and the outstanding properties of high strength and stiffness for pure Cu, Fe–Cu alloys possess their advantages and display a prosperous application prospect in the fields of electrical materials and structural materials.[1–7] Since binary Fe–Cu alloys have a large positive mixing enthalpy, metastable phase separation usually occurs inside this kind of alloy when it solidifies under the non-equilibrium solidification condition.[2,7] How to modulate the metastable phase separation and subsequent solidification process to optimize their related mechanical and electrical properties has become a hot topic in recent years.[1–9] Previous investigations about the Fe–Cu alloys mainly concentrated on two aspects. In the first aspect, many attempts have been made to clarify the effects of cooling rate,[8–10] undercooling level,[2,11,12] melt convection[13–15] and high magnetic field[13,16] on

the metastable phase separation and microstructure evolution by using a series of advanced solidification techniques, such as the drop tube,[15,17] gas atomization,[6,18] laser powder bed fusion,[19,20] melt spinning[21,22] and high undercooling[2,5,11,12,16,23–26] and so on. The numerical simulations are also employed to understand metastable phase separation kinetics of Fe–Cu alloys under various conditions.[2,5,11,15] So far, both experiments and simulations are widely conducted to elucidate the scientific laws of metastable phase separation under the extremely non-equilibrium solidification condition. On the other hand, the optimization of related performance for Fe–Cu alloys is mainly accomplished by the addition of third element of Zr, Mg, Ag, W, Si, Nb, V, C and B.[4,27–34] It was found that the addition of third element could manipulate the mechanical property, electrical property and magnetic property of Fe–Cu alloy materials. Nevertheless, there are very limited studies about the manipulations of micromechanical property and electrical property via

controlling solidification processes. The relationship between dominant parameters of solidification process control and the applied properties of Fe–Cu alloys remains elusive, and conducting this aspect of research is of great importance in both scientific and industrial fields.

The glass fluxing technique provides a chance to modulate the undercooling level of liquid Fe–Cu alloys in a wide range.[2,5,11,12,15] To explore the variations of micromechanical and electrical properties with the undercooling level, this work selects a model alloy of $Fe_{87}Cu_{13}$ as a research object, in which the proportion of iron and copper is relatively suitable for the simultaneous investigations of metastable phase separation and applied properties under the highly undercooled state. In the present work, the microstructural hardening mechanisms and electrical property manipulations of undercooled $Fe_{87}Cu_{13}$ alloy have been investigated by systematical characterizations of Vickers microhardness and electrical impedance for glass-fluxed samples. Special attentions are paid to understand the solidification kinetics, microstructure evolution as well as the variation of Vickers microhardness and electrical impedance with the undercooling level.

II. METHODOLOGY

A. Glass Fluxing Experiment

Every master alloy of $Fe_{87}Cu_{13}$ with a mass of about 0.6 g was prepared by the arc melting method in an argon protecting environment. The master alloy and some appropriate amount of fluxing agent (80 pct SiO_2 + 20 pct $Na_2B_4O_7$) were placed in a cylindrical alumina crucible with a height of 8 mm and a bottom diameter of 8 mm, which was subsequently installed inside a vacuum chamber. Before the glass fluxing experiment, the vacuum chamber was first evacuated to 2.8×10^{-4} Pa and then backfilled with argon gas to 70 kPa. The crucible with both the sample and fluxing agent was pushed inside an induction coil. Using the induction heating technique, the melting and overheating of the Fe–Cu alloy sample could be completed successively. Afterwards, the alloy sample cooled gradually as the heating power was cut off, and it may obtain an undercooling state before the nucleation and growth of primary phase. To obtain the typical desired undercooling level, the heating and cooling of the samples during the glass fluxing experiment were repeated several times. The sample temperature signals was monitored by a two-color pyrometer (CHINO IR-CZ) with an absolute accuracy of ± 5 K. The recalescence process was detected by a high-sensitivity photodiode (Thorlabs PDA 100A-EC).

The undercooled samples were ground and polished. The solidification microstructures were characterized by an FEI Sirion Electron Microscope together with a high resolution camera (Redmi K40). The Vickers microhardness of undercooled $Fe_{87}Cu_{13}$ alloy was measured at room temperature by a Microhardness Tester (HXP-1000TM) with a load of 0.98 N and a dwell time of 10 s. In a frequency range of 10^{-2} to 10^5 Hz, the electrical property of undercooled samples was analyzed by an Electrochemical Workstation (Wuhan Koster CS350), in which a dielectric solution of NaCl with a concentration of 3.5 wt pct was used.

B. Numerical Simulation

In this work, metastable phase separation (MPS) occurs once the $Fe_{87}Cu_{13}$ alloy was undercooled beyond 244 K. To study the MPS process in glass fluxing experiment, the effects of surface segregation, Marangoni convection and Stokes motion were additionally considered in the Shan-Chen model.[35,36] The supplemented equations of additional three effects are given as follows:

$$\mu(\mathbf{x}) = V(\mathbf{x},\mathbf{x}') + \xi \cdot \psi^j_S(\mathbf{x}) + \psi^j_T(\mathbf{x}) \qquad [1]$$

$$\psi^j_S(\mathbf{x}) = H - Q \cdot \rho^j(\mathbf{x})|_{\mathbf{x}_S} \qquad [2]$$

$$\psi^j_T(\mathbf{x}) = -\ln\left(\frac{\rho^j + \zeta}{\rho - \rho^j - \zeta}\right) \cdot T \qquad [3]$$

$$\delta f^j_i(\mathbf{x}, t) = \frac{n_{L_1} - n_{L_2}}{4} \cdot \frac{e_{i,y}}{|e_{i,y}|} \cdot \frac{|\mathbf{g}|\Delta t}{c} \quad i = 0, 1, 2, \ldots, 8 \quad [4]$$

$$\sum\nolimits_{i=0}^{8} \delta f^1_i(\mathbf{x}, t) = 0 \qquad [5]$$

$$\sum\nolimits_{i=0}^{8} \delta f^1_i(\mathbf{x}, t) \cdot \mathbf{e}_i = (n_{L_1} - n_{L_2}) \cdot \mathbf{g} \cdot \Delta t \qquad [6]$$

$$\sum\nolimits_{j=1}^{2} \delta f^j_i(\mathbf{x}, t) = 0 \qquad [7]$$

where $\psi^j_S(\mathbf{x})$, $\psi^j_T(\mathbf{x})$ and $\delta f^j_i(\mathbf{x}, t)$ are additional effects caused by the surface segregation, Marangoni convection and Stokes sedimentation. Besides, $V(\mathbf{x}, \mathbf{x}')$ is the interaction potential between the liquid L_1 and L_2 phases in Shan-Chen model, ξ is set to be 1.0 at the boundary while it is taken as 0 at other places, ζ is the tiny perturbation, T is the temperature, H and Q are the corresponding parameters of surface segregation, n_{L_1} and n_{L_2} are the densities of liquid phases L_1 and L_2, $\mathbf{g}$ is the gravity acceleration, Δt is time step, c is the lattice velocity, $\mathbf{e}_i$ is the movement velocity in i direction, and $e_{i,y}$ is the y-direction component of particle velocity in the i-th direction. The details of this lattice Boltzmann model can be found elsewhere.[5]

III. RESULTS AND DISCUSSION

A. *Cooling Curve Analyses*

Through repeating glass fluxing experiments, liquid $Fe_{87}Cu_{13}$ alloy was substantially undercooled up to 399 K (0.23 T_L). The critical undercooling for the occurrence of metastable phase separation is experimentally determined as 244 K, which is a little greater than the theoretically predicted 236 K undercooling[12] as plotted by a green circle in Figure 1. The following metallurgical observations demonstrate the existence of two solidification modes, which are named as NPS mode and PS mode. For the convenience of subsequent discussions, NPS mode and PS mode should be defined first. The PS mode denotes the mode in which liquid phase separation occurs before the nucleation of primary phase, whereas NPS mode represents the mode in which liquid phase separation does not happen prior to primary phase solidification. As the undercooling is higher than 244 K, PS mode would be selected and metastable phase separation happens. As the undercooling is less than 244 K, the NPS mode prevails, indicating that metastable phase separation doesn't occur and the typical peritectic solidification microstructure forms finally.

Figure 2(a) shows the typical cooling curves of glass-fluxed $Fe_{87}Cu_{13}$ alloy. Clearly, there are two exothermic peaks on the cooling curves in both NPS mode and PS mode. Based on binary Fe–Cu phase diagram, it can be known that the first peak represents the nucleation and growth of primary γFe phase and the second peak denotes the solidification of (Cu) phase under the condition of NPS mode. Moreover, with a rise in the undercooling, the first recalescence becomes more and more apparent. As the undercooling level is improved above 244 K, NPS mode transforms into the PS mode and metastable phase separation takes place. In this case, there should be three exothermic peaks instead of two peaks on the cooling curves. The first one should be caused by the occurrence of metastable phase separation, the second and third ones are resulted from

the solidification of γFe and (Cu) phases. The reason why the first peak is not observed is that latent heat produced by the metastable phase separation of $Fe_{87}Cu_{13}$ alloy is too little to be detected. For the NPS mode and PS mode, many related experimental evidences of undercooled Fe–Cu alloys[11,12] show that γFe phase ultimately changes into the αFe phase if the temperature further decreases to the room temperature.

To explore the effect of copper proportion for Fe–Cu alloy on the exothermic peaks caused by the metastable phase separation and the solidification of (Cu) phase, a comparison of both cooling curve and solidification morphology between $Fe_{87}Cu_{13}$ and $Fe_{65}Cu_{35}$ alloys is displayed in Figure 2(b). According to the metallurgical observations, metastable liquid phase separation occurs for both $Fe_{87}Cu_{13}$ alloy (ΔT = 325 K) and $Fe_{65}Cu_{35}$ alloy (ΔT = 332 K). Nevertheless, the macrosegregation phenomenon induced by metastable phase separation of 332 K undercooled $Fe_{65}Cu_{35}$ alloy is more conspicuous than that for 325 K undercooled $Fe_{87}Cu_{13}$ alloy, as observed in the inserted macrosegregation morphologies of Figure 2(b). In contrast with the relatively smooth curve before the nucleation of primary phase for 325 K undercooled $Fe_{87}Cu_{13}$ alloy, there is an inflection point on cooling curve prior to the primary phase solidification of 332 K undercooled $Fe_{65}Cu_{35}$ alloy. Furthermore, the thermal plateau of the solidification for (Cu) phase inside $Fe_{65}Cu_{35}$ alloy is longer than that for $Fe_{87}Cu_{13}$ alloy. It can be concluded that the latent heats caused by the metastable phase separation and the solidification of (Cu) phase for $Fe_{65}Cu_{35}$ alloy are much more than that for $Fe_{87}Cu_{13}$ alloy. It can be concluded that the copper proportion of undercooled Fe–Cu alloy greatly influences the exothermic peaks caused by the metastable phase separation and the solidification of (Cu) phase. As the copper proportion of $Fe_{87}Cu_{13}$ alloy is only 13 at pct, metastable phase separation phenomenon is not so obvious even in highly undercooled state, and naturally the exothermic peak caused by the metastable phase separation is too small to be observed on the cooling curve.

B. *Rapid Dendrite Growth Characteristics*

The glass fluxing technique has proven to be an efficient approach to measure the dendrite growth velocity of undercooled alloys.[12] The dendritic growth velocity is usually determined by the equation of $D/\Delta t$, in which D is the largest diameter of the sample and the Δt is the rapid recalescence time.[11,12,25,26] The hollow red circles in Figure 3(a) stand for the measured growth velocity of primary γFe phase in undercooled $Fe_{87}Cu_{13}$ alloy. At a small undercooling of 55 K, primary dendrite growth velocity is only 1.1 m/s. A rise in the undercooling contributes to the continuous enhancement of primary dendrite growth velocity. When the undercooling attains the maximum value of 399 K, primary dendrite growth velocity increases up to 22.0 m/s. This implies that a high undercooling accelerates the rapid growth of primary γFe dendrites. In addition, primary dendrite growth velocities of undercooled $Fe_{92.8}Cu_{7.2}$
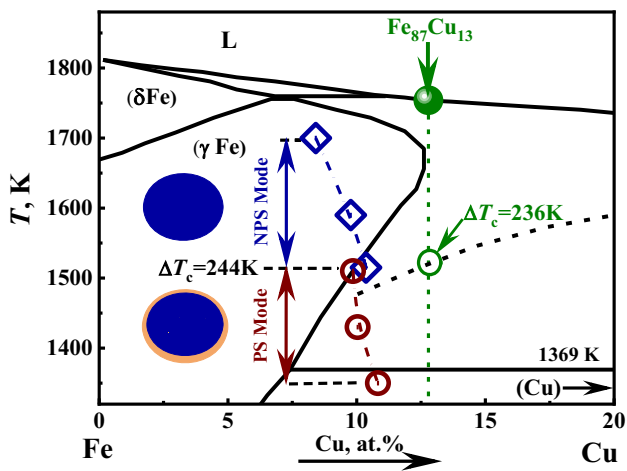

Fig. 1—(Color online) Solidification mode determinations and copper content inside αFe phase of selected model $Fe_{87}Cu_{13}$ alloy designated in binary Fe–Cu phase diagram.
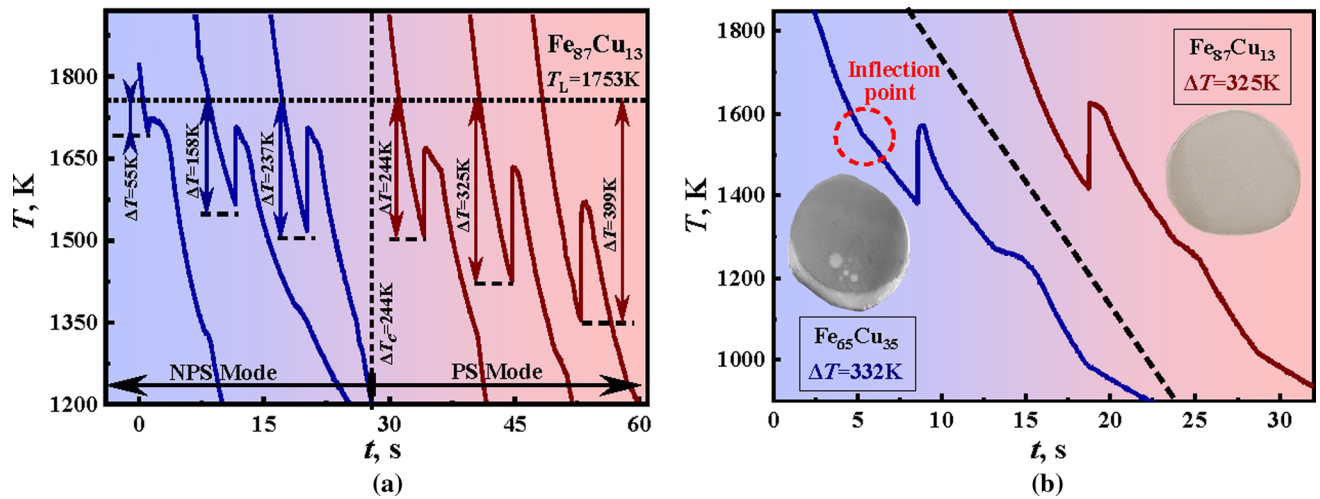
Fig. 2—(Color online) Analyses of thermal history for glass-fluxed Fe–Cu alloys: (*a*) cooling curves of Fe$_{87}$Cu$_{13}$ alloy, (*b*) a comparison of both cooling curve and solidification morphology between Fe$_{87}$Cu$_{13}$ and Fe$_{65}$Cu$_{35}$ alloys.
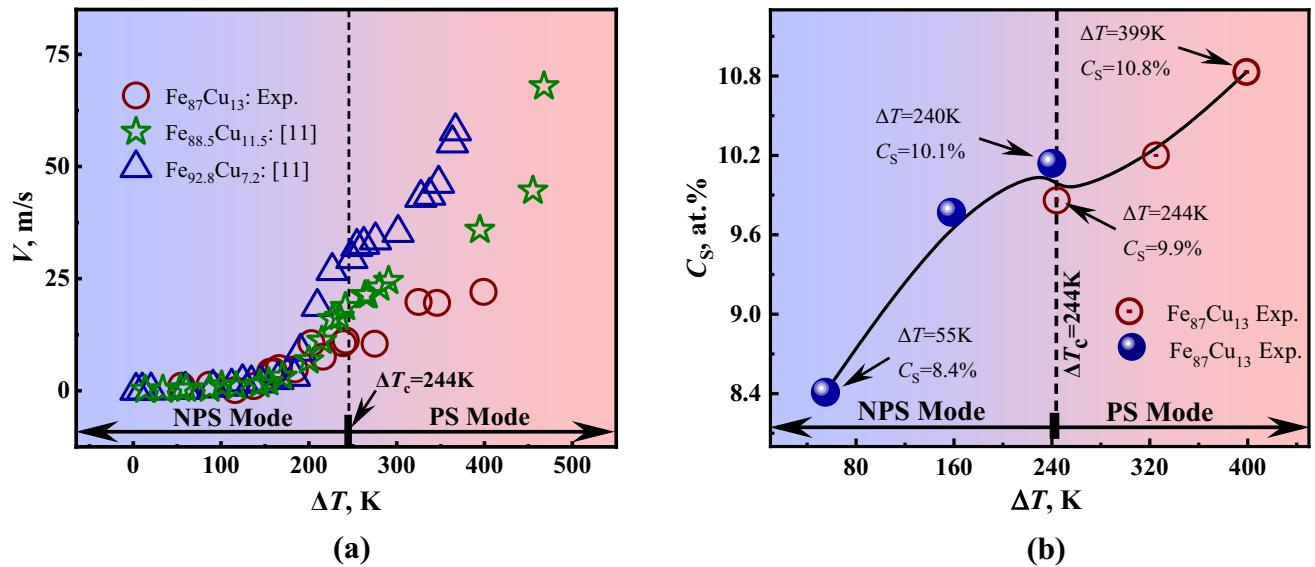

Fig. 3—(Color online) Rapid dendrite growth characteristics for undercooled Fe–Cu alloys: (*a*) dendrite growth velocity of primary γFe phase, (*b*) the copper content inside the αFe dendrites of Fe$_{87}$Cu$_{13}$ alloy.

and Fe$_{88.5}$Cu$_{11.5}$ alloys could be obtained from the Reference 11 and their values are also plotted in Figure 3(a) for a comparison with undercooled Fe$_{87}$Cu$_{13}$ alloy. Obviously, primary dendrite growth velocities of these three Fe–Cu alloys always show an upward trend with the enlarged undercooling. As the copper proportion of Fe–Cu alloys increases from the 7.2 to 13 at pct, the growth velocity of primary dendrites shows a decreasing trend at the same undercoolings and the magnitude of the decrease in growth velocity is more significant under a higher undercooling condition.

As the growth of primary dendrites is drastically accelerated in highly undercooled state, the copper content inside those αFe dendrites maybe increases owing to the remarkable solute trapping effect. To ensure the data reliability of the copper content, the copper content is measured by the point analysis of

EDS. For every undercooling, we measure the average Cu content of 15 experimental points in the middle regions of 15 different αFe dendrite grains. Figure 3(b) presents the copper content inside the αFe dendrites at different undercoolings. Apparently, if the metastable phase separation does not happen, *i.e.* the melt undercooling is lower than 244 K, the copper content inside αFe dendrites enhances from 8.4 at pct at $\Delta T = 55$ K to 10.1 at. pct at $\Delta T = 240$ K. Once the increasing undercooling approaches to 244 K, the copper content inside αFe dendrites shows a sudden drop from 10.1 to 9.9 at pct. In this case, metastable phase separation occurs, Cu-rich liquid flows to the sample surface to form a Cu-rich shell due to the surface segregation, and the copper inside the sample decreases naturally. This may explain an abrupt drop of the copper content in αFe dendrites at this critical

undercooling for the occurrence of metastable phase separation. As the undercooling increases further, metastable phase separation is always observed. In addition, the copper content inside αFe dendrites becomes more and more, and attains to 10.8 at pct at the maximum undercooling of 399 K.

C. Solidification Microstructure Evolution

Figure 4 shows the solidification microstructure evolution of undercooled $Fe_{87}Cu_{13}$ alloy, in which the dark color denotes the αFe phase and the bright color represents the (Cu) phase. As liquid $Fe_{87}Cu_{13}$ alloy solidifies with a small undercooling of 55 K, αFe phase appears as well-defined coarse dendrites and the (Cu) phase distributes in the region of grain boundary, as seen in Figure 4(a). With the enhancement of the undercooling to 240 K, the solidification microstructure refines greatly as seen in Figure 4(b). If the undercooling is further enhanced by 4 K, a Cu-rich shell with a thickness of about 2.9 μm occupies the surface region of 244 K undercooled sample as shown in Figure 4(c), indicating that metastable phase separation begins to arise. The (Cu) phase inside 244 K undercooled sample still locates in the grain boundary, and its morphology is mainly characterized by fiber-like or granular shape, as displayed in Figure 4(d). As the undercooling rises to the maximum value of 399 K, metastable phase separation comes into being, and results in the formation of a Cu-rich surface segregation layer with a thickness of approximate 3.6 μm, as presented in Figure 4(e). The microstructure enlargement of Zone B in Figure 4(e) is given in Figure 4(f). The microstructure displays a network morphology of grain boundaries without discernible dendrites, and most of (Cu) phase inside the sample possesses granular shape.

As three effects of surface segregation, Marangoni migration and Stokes motion are taken into account in the above lattice-Boltzmann model, metastable liquid phase separation process of $Fe_{87}Cu_{13}$ alloy is simulated in Figure 5. Before the simulations, the sample shape is supposed to have a spherical shape with a dimensionless diameter of 130 Δx for the simplification of simulation. Here, Δx is the space step and it is taken as 1.0, whereas the time step Δt is also set as 1.0. The surface segregation parameters H and Q are respectively given as 0.38 and 0.10. The interaction coefficient is G_0 set as $-$ 1.20. Both the relaxation times of Fe-rich and Cu-rich liquids are taken as 1.0. The gravity acceleration velocity g and the densities of Fe-rich and Cu-rich liquids used in the simulations are set as 9.8 m/s^2, 7030 kg/m^3 and 8000 kg/m^3,[37] respectively. To introduce the thermal Marangoni convection in the phase separation process, the temperature at the sample center is set as 0.8 T_L and it decreases linearly from the center to the droplet surface. Moreover, the temperature interval between the center and the surface of the sample is taken as 0.03 T_L.

Since the copper proportion in $Fe_{87}Cu_{13}$ alloy is relatively low, the volume of Cu-rich liquid separated from the homogeneous alloy melt is very small during the metastable phase separation, as simulated in Figures 5(a) and (b). Due to the smaller surface energy of Cu-rich liquid in contrast with that of Fe-rich liquid, Cu-rich liquid phase flows towards sample surface to decrease the system energy, and forms a very thin Cu-rich shell as shown in Figures 5(b) and (c). Meanwhile, because the undercooling at sample surface is a little larger than that inside the sample, the secondary Cu-rich liquid phase has a tendency to preferentially be separated from the parent liquid phase at the region of the sample surface. The two dominant mechanisms are responsible for the migration of Cu-rich liquid towards to sample surface and the formation of Cu-rich surface
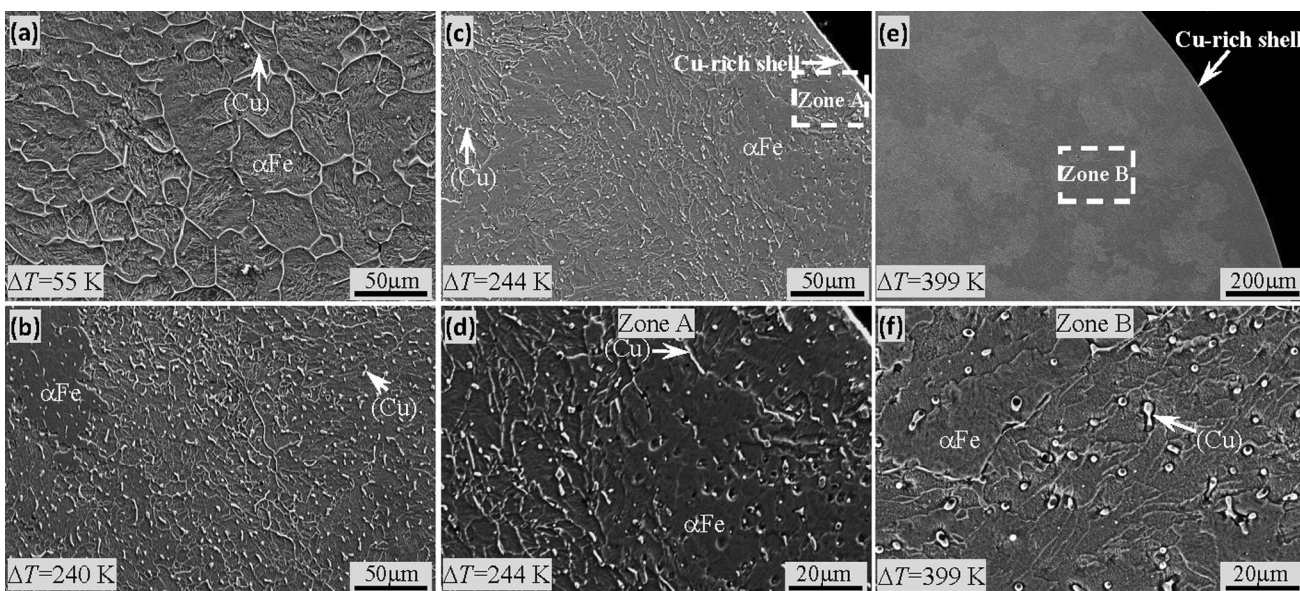

Fig. 4—(Color online) Solidification microstructure evolution of undercooled $Fe_{87}Cu_{13}$ alloy: (a) $\Delta T = 55K$, (b) $\Delta T = 240K$, (c) and (d) $\Delta T = 244K$, (e) and (f) $\Delta T = 399K$.

(a) τ=2 steps   **(b)** τ=100 steps   **(c)** τ=500 steps   **(d)** τ=2000 steps
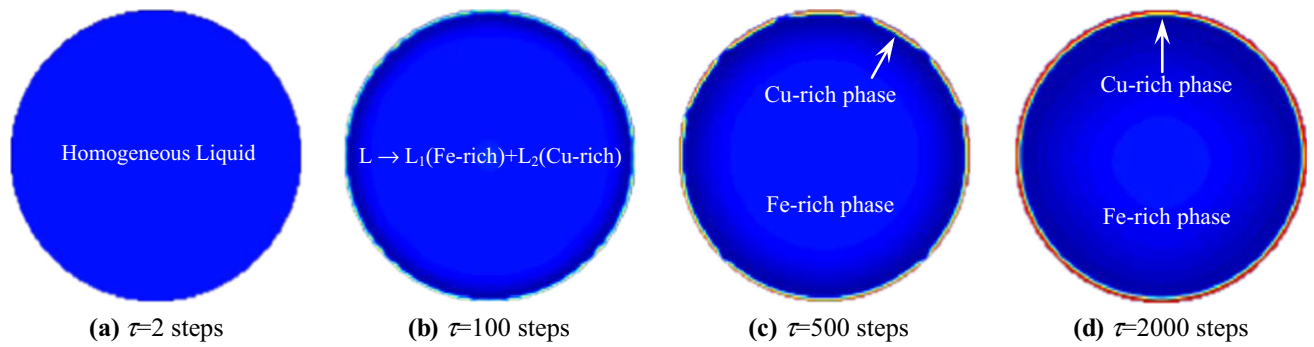
Fig. 5—(Color online) Numerical simulations for metastable phase separation process of binary $Fe_{87}Cu_{13}$ alloy: (a) through (d) correspond to the snapshots of metastable liquid phase separation at dimensionless evolutionary time τ of 2 steps, 100 steps, 500 steps and 2000 steps.
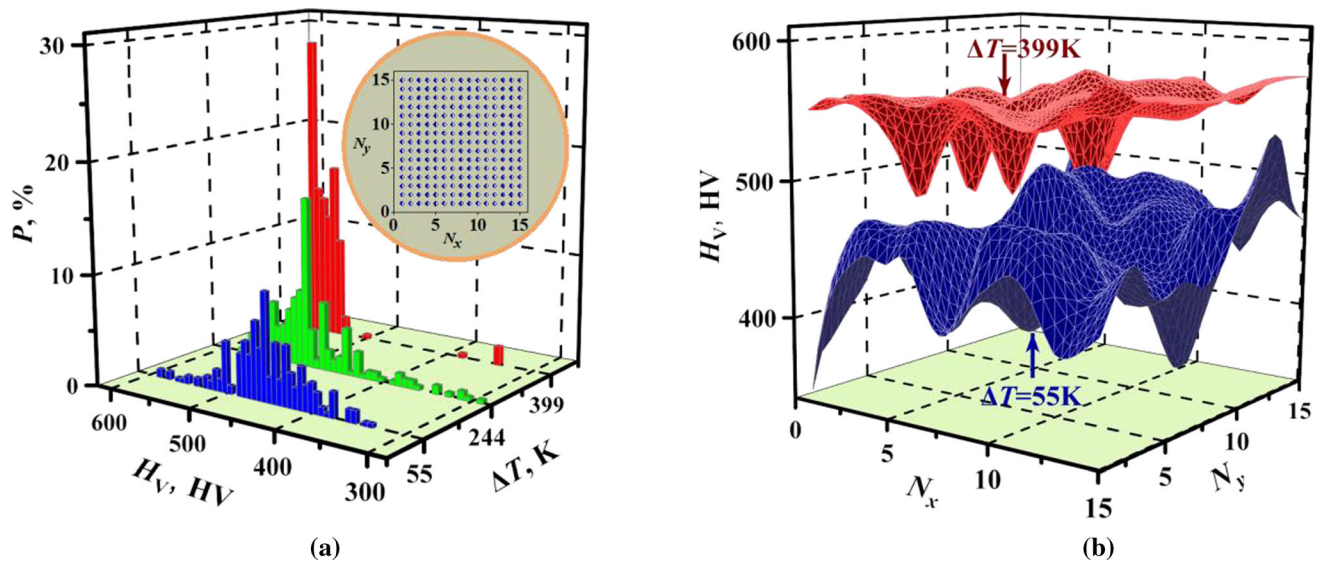

(a)   **(b)**

Fig. 6—(Color online) Vickers microhardness measurement of undercooled $Fe_{87}Cu_{13}$ alloy: (a) distribution probability of Vickers microhardness, (b) mapping of Vickers microhardness.

segregation layer. As the evolutionary time extends, Cu-rich surface segregation shell becomes thicker as observed in Figure 5(d). The simulated morphology agrees well with the experimental observations in Figures 4(c) and (e). Since the dispersed secondary globules of Cu-rich phase is difficult to be separated from the matrix phase inside the sample, the influences of thermal Marangoni convection and Stokes sedimentation on the metastable phase separation are so weak that they are difficult to be identified in both experiments and simulations. This also demonstrates that the surface segregation effect on the liquid phase separation is more obvious than the influences of the thermal Marangoni convection and the Stokes motion when the copper proportion of Fe–Cu alloy is relatively small.

D. *Microstructural Hardening Mechanisms*

To further analyze the microstructural hardening mechanisms, the Vickers microhardness of $Fe_{87}Cu_{13}$ alloy is systematically measured at various undercoolings, and the obtained data are illustrated in Figure 6. As for each undercooled sample, a square region locating in the middle region of the sample is selected to test the Vickers microhardness. The schematic of this square region consisting of 225 experimental points can be seen clearly from the inserted figure in Figure 6(a), and the distance between the neighboring test points is about 50 μm. Here, N_x and N_y represent the column number and line number for the matrix of 225 experimental test points, respectively. Figure 6(a) shows the probability distribution of Vickers microhardness for three typical undercooled $Fe_{87}Cu_{13}$ alloys. As the

undercooling equals 55 K, the measured microhardness is not homogeneous. The peak value of microhardness distribution spectra attains 9.8 pct and this peak locates within the microhardness range of 445 to 455 HV. With increasing undercooling to 244 K, the microhardness distribution spectra still displays non-homogeneous characteristics. In contrast with the 55 K undercooled $Fe_{87}Cu_{13}$ alloy sample, the peak value of microhardness distribution spectra rises to 15.6 pct, which corresponds to the appearance probability of the microhardness within the range of 490 to 500 HV. As the undercooling further enhances to the maximum value of 399 K, the microhardness distribution spectra is relatively homogeneous in comparison to the previous two ones. In such a case, the peak value of microhardness distribution spectra becomes larger and approaches to 28.5 pct in the microhardness range of 560 to 570 HV. Figure 6(b) depicts the three-dimensional mapping results of microhardness for undercooled $Fe_{87}Cu_{13}$ alloy. Evidently, the microhardness of 399 K undercooled sample is much greater than that for 55 K undercooled sample. Moreover, the homogenization level of measured microhardness for previous one is higher than that for the latter one. The metallurgical observations show that the measured microhardness will generally be smaller than other regions if the location of test point is just near the (Cu) phase with a lower microhardness, which is also consistent with the results in Reference 2. Besides, it is also possible that the defects (such as voids) on those regions are responsible for the sudden drop of hardness at various locations. These reasons may explain the phenomenon that the microhardness at some positions decreases sharply, as shown in Figure 6(b). It can be concluded that a higher undercooling contributes to not only the enhancement in the microhardness but also the homogenization of the microhardness.

Figure 7(a) presents the average Vickers microhardness of $Fe_{87}Cu_{13}$ alloy at different undercoolings. At a slight undercooling of 55 K, average Vickers microhardness is only 451.1 HV. In small undercooling regime below 240 K, a rise in the undercooling leads to the continuous improvement of the Vickers microhardness. As the undercooling increases from 240 K to 244 K, the Vickers microhardness displays a sudden drop from 503.0 HV to 490.7 HV, which is closely related to the occurrence of metastable liquid phase separation and it will be interpreted in the following. With the further enhancement of the undercooling, the microhardness starts to rise again and attains to 552.4 HV at the largest undercooling of 399 K. The average microhardness is enhanced by 22.5 pct in contrast with 55 K undercooled sample.

The variations of microhardness with the copper content in the αFe phase and the primary dendrite growth velocity are also explored and their relationships are respectively plotted in Figures 7(b) and (c). Obviously, under the solidification modes of both NPS and NPS, the average Vickers microhardness increases with the increment of the copper content in αFe phase. As the solidification mode transforms from NPS mode to PS mode, the copper content in αFe phase decreases abruptly. This results in the reduction of the average Vickers microhardness. Therefore, the enhancement of copper content in αFe phase helps to improve the microhardness of undercooled $Fe_{87}Cu_{13}$ sample.

In both NPS mode and PS mode, the average Vickers microhardness shows an upward trend as the growth of primary dendrites is considerably accelerated, as seen in Figure 7(c). In other words, the faster the growth of primary dendrite the finer the solidification microstructure and the greater the microhardness of the sample would be. As the undercooling rises from 240 K to 244 K, primary dendrite growth velocity varies from 10.6 to 11.2 m/s. The weak rising variations of both melt undercooling and dendrite growth velocity have little impact on the solidification refinement. In principle, average Vickers microhardness of the sample should display a very small upward trend that can hardly be identified. Nevertheless, this speculation is inconsistent with the measured data in Figure 7(c). As the NPS mode just changes into the PS mode, the rise in the growth velocity of primary dendrites is very small, and the microstructure refinement can be almost ignored. In this case, the sudden drop of copper content in αFe phase is responsible for an abrupt reduction of microhardness. Thus, melt undercooling plays a crucial role in the sample microhardness. Although the cooling rate also influences the Cu content in the αFe phase as well as the grain size, the average cooling rates of glass-fluxed samples are very close in this work, and the cooling rate has a little effect on the sample microhardness in the present work. The variations of primary dendrite growth velocity, grain size and the copper content in primary solid mainly dominate the evolution tendency of the microhardness for the undercooled $Fe_{87}Cu_{13}$ alloy.

E. Electrical Property Manipulations

Figure 8(a) shows Nyquist plot of electrochemical impedance spectroscopy (EIS) for undercooled $Fe_{87}Cu_{13}$ alloy. Obviously, the undercooling level greatly influences the Nyquist plot of the EIS. In small undercooling regime below 244 K, the enhanced undercooling leads to an enlargement of impedance semicircle. As the undercooling rises to 244 K, the impedance semicircle becomes smaller suddenly. Subsequently, with the further rise in the undercooling, impedance semicircle is gradually getting bigger. Considering that the size of impedance semicircle is closely related to the impedance, the undercooling variation plays a crucial role in the impedance of undercooled $Fe_{87}Cu_{13}$ alloy. In other words, by modulating the undercooling level, the charge transfer characteristics in those undercooled alloys can be manipulated according to the undercooling dependence of the impedance, so as to actively control the electrical property.

To investigate the undercooling effect on the impedance characteristics, an equivalent circuit inserted in Figure 8(a) needs to be established to first fit those experimental data of the Nyquist plot. The consistency of fitting curves and experimental data demonstrates the rationality and correctness of simulated equivalent circuit. Here, Rs is the solution resistance of dielectric
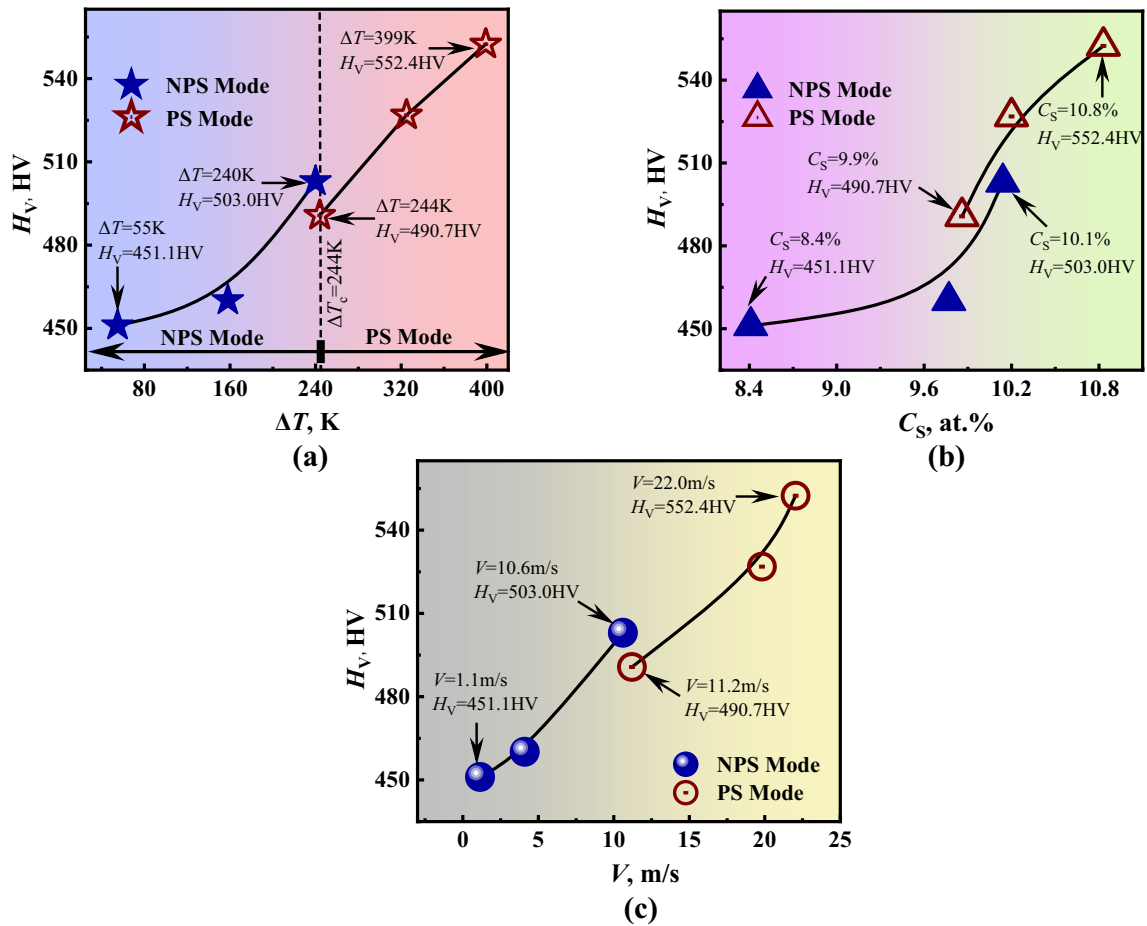
Fig. 7—(Color online) Microstructural hardening mechanisms of undercooled $Fe_{87}Cu_{13}$ alloy: (*a*) undercooling effect on the Vickers microhardness, (*b*) the relationship between the Vickers microhardness and copper content inside αFe dendrites, (*c*) the variation relation of Vickers microhardness with the growth velocity of primary γFe dendrites.

solution, Rp is the polarization resistance, and CPE is the double-layer capacitance. It should be noted that the solution resistance of dielectric solution is very small and the undercooling has little influences on the solution resistance. The very small distinctions of the solution resistance during the measurement of these undercooled samples are mainly caused by the systematic error of experimental measurement.

From the equivalent circuit and Nyquist plot in Figure 8(a), the polarization resistance Rp and the two important parameters of the double-layer capacitance CPE including the capacitance CPE-T and the phase angle φ can be determined accordingly. The corresponding results versus bulk undercooling are plotted in Figures 8(b), (c) and (d). Provided that the undercooling changes from 55 K to 240 K, the grain boundaries gradually increase due to the greatly refined solidification microstructure, and meanwhile the crystal defects and vacancies become more. The above variations may enhance the scattering of free electrons as the electrons transfer in the alloy.[38] Naturally, this makes the electrical resistance become larger. Specifically,

polarization resistance Rp is enhanced from 1478 Ω to 1660 Ω while the capacitance CPE-T also presents an increasing trend from 1.0 to 4.2 mF. As the enlarged undercooling attains the 244 K, metastable phase separation occurs and results in the migration of Cu-rich liquid phase towards to the sample surface to form a Cu-rich shell. As a result, the fiber-like (Cu) phase locating in the region of grain boundaries remarkably reduces and moreover some of (Cu) phase transforms into the granular morphology. All these variations perhaps weaken the scattering effects of free electrons, which may induce a sudden drop for the polarization resistance and the capacitance at this threshold undercooling of 244 K. As the undercooling continues to rise, both the polarization resistance and capacitance are gradually enhanced owing to the enhancement of free electron scattering caused by the more grain boundaries and solidification defects. The undercooling influence on the phase angle is so tiny that it can be ignored. In undercooling range of 55 to 399 K, the phase angle basically remains a constant of − 73.5 deg.
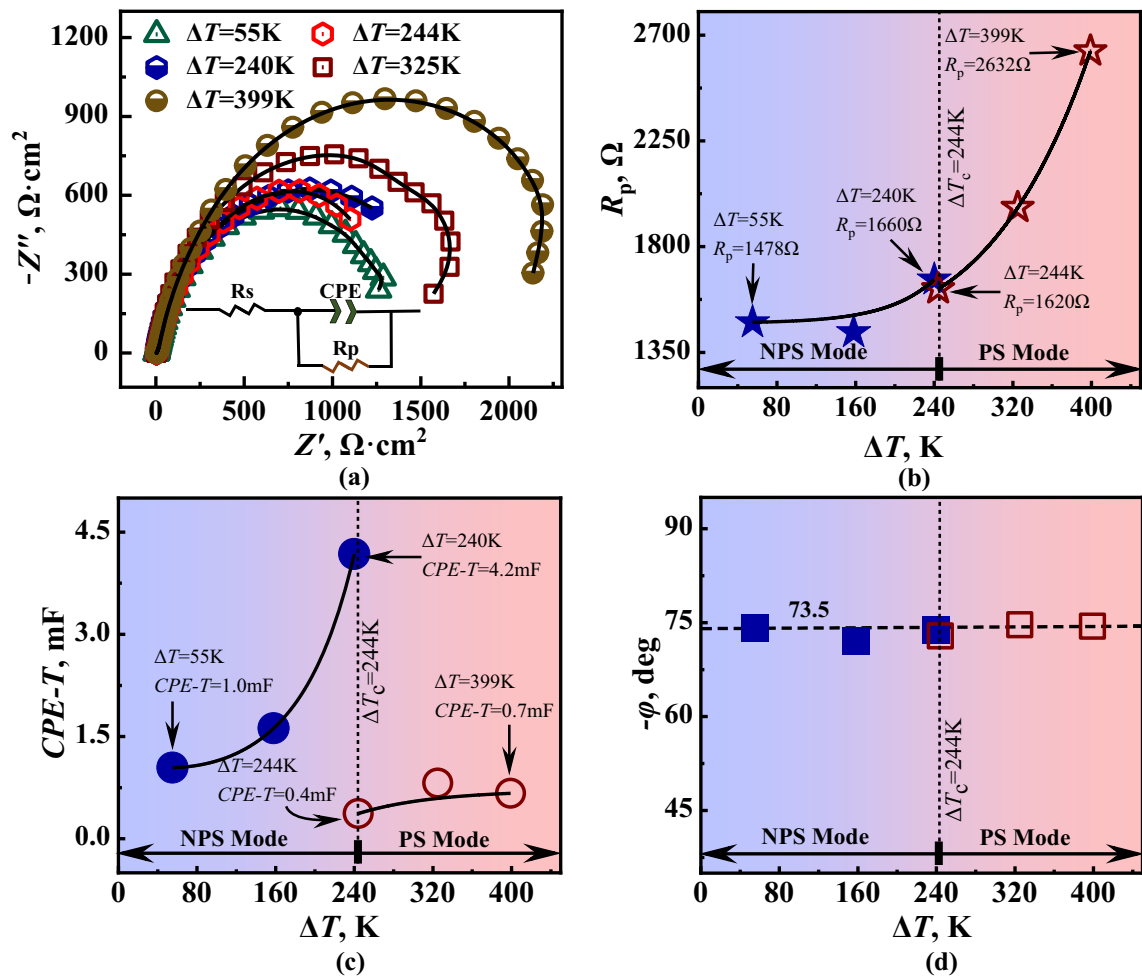
Fig. 8—(Color online) Impedance characteristics analyses of undercooled $Fe_{87}Cu_{13}$ alloy: (*a*) Nyquist plots for differently undercooled alloys, (*b*) electric resistance versus bulk undercooling, (*c*) undercooling effect on the electrical capacity, (*d*) the variation relation of phase angle with the bulk undercooling.

IV. CONCLUSIONS

In summary, using the glass fluxing method, liquid $Fe_{87}Cu_{13}$ alloy is easy to be undercooled and the obtained undercooling locates between 55 K and 399 K. The critical undercooling for the occurrence of metastable phase separation is determined as 244 K in the experiments. Peritectic solidification happens at slight undercoolings below 244 K, and the phase-separated morphologies with a Cu-rich shell are observed at high undercoolings above 244 K. As the undercooling level becomes larger, a conspicuous microstructure refinement takes place, and primary dendrite growth velocity displays an upward trend and attains 22.0 m/s at the maximum undercooling of 399 K. When the proportion range of Cu element in Fe–Cu alloys is between 7.2 and 13 at pct, the enhancement of copper proportion suppresses the rapid growth of primary dendrites to some extent, especially in highly undercooled state. Due to the occurrence of metastable phase separation, a sudden drop of copper content in αFe dendrites arises at a critical undercooling of 244 K. In the small undercooling regime below 244 K and the large undercooling regime above 244 K, the copper content in αFe dendrites is enhanced with the undercooling. The metastable phase separation process of $Fe_{87}Cu_{13}$ alloy is reproduced by a lattice-Boltzmann model. The simulated results show that the effects of Stokes motion and Marangoni migration on the phase separation process are very weak since the copper proportion of $Fe_{87}Cu_{13}$ alloy is relatively low. In this case, surface segregation mainly controls liquid phase separation process and contributes to the formation of a Cu-rich shell. The characterizations of Vickers microhardness and electrical impedance reveal that the undercooling plays an important role in Vickers microhardness and electrical impedance. The higher the undercooling the larger the Vickers microhardness and electrical impedance they are. Experimental results and theoretical analyses demonstrate that the dendrite growth velocity, solute content and grain size of primary phase greatly influence the microhardness while the magnitude of electrical impedance is closely related to the number of grain boundaries, crystal defects and vacancies.

COMPETING INTEREST

The authors declare that they have no known competing financial interests or personal relationships that could have appeared to influence the work reported in this paper.

REFERENCES

1. X.X. Lv, N. Cao, L.J. He, B. Liu, H.T. Sun, W.T. Qiu, Z. Xiao, Y.B. Jiang, and S. Gong: *Mater. Charact.*, 2023, vol. 196, 112612.
2. Y.H. Wu, B.R. Zhu, H.L. Du, Z.C. Xia, J.W. Su, and Z.M. Gao: *J. Alloy. Compd.*, 2022, vol. 913, 165268.
3. C.Z. Zhang, C.G. Chen, P. Li, M.J. Yan, Q. Qin, F. Yang, W.W. Wang, Z.M. Guo, and A.A. Volinsky: *J. Alloy. Compd.*, 2022, vol. 909, 164761.
4. S.C. Liu, J.C. Jie, Z.K. Guo, S.P. Yue, and T.J. Li: *Mater. Chem. Phys.*, 2019, vol. 238, 121909.
5. Y.H. Wu, B.R. Zhu, H.L. Du, Z.M. Gao, X. Zhao, and Y.H. Bai: *Metall. Mater. Trans. A*, 2022, vol. 53A, pp. 4377–92.
6. J. He, J.Z. Zhao, and L. Ratke: *Acta Mater.*, 2006, vol. 54(2006), pp. 1749–57.
7. D. Watanabe, C. Watanabe, and R. Monzen: *Acta Mater.*, 2009, vol. 57, pp. 1899–1911.
8. Y.H. Wu, B.R. Zhu, J.W. Su, Z.M. Gao, and X. Zhao: *J. Alloy. Compd.*, 2022, vol. 927, 167079.
9. S.C. Liu, J.C. Jie, Z.K. Guo, G.M. Yin, T.M. Wang, and T.J. Li: *J. Alloy. Compd.*, 2018, vol. 742, pp. 99–106.
10. S.C. Liu, J.C. Jie, B.W. Dong, Z.K. Guo, T.M. Wang, and T.J. Li: *Mater. Des.*, 2018, vol. 156, pp. 71–81.
11. Z.C. Xia, W.L. Wang, S.B. Luo, and B. Wei: *Chem. Phys. Lett.*, 2016, vol. 658, pp. 220–23.
12. S.B. Luo, W.L. Wang, J. Chang, Z.C. Xia, and B. Wei: *Acta Mater.*, 2014, vol. 69, pp. 355–64.
13. E. Shoji, S. Isogai, R. Suzuki, M. Kubo, T. Tsukada, T. Kai, T. Shinohara, Y. Matsumoto, and H. Fukuyama: *Scr. Mater.*, 2020, vol. 175, pp. 29–32.
14. W. Li, H.X. Jiang, L.L. Zhang, S.X. Li, J. He, J.Z. Zhao, and F. Ai: *Scr. Mater.*, 2019, vol. 162, pp. 426–31.
15. Y.H. Wu, W.L. Wang, J. Chang, and B. Wei: *J. Alloy. Compd.*, 2018, vol. 763, pp. 808–14.
16. Y.K. Zhang, J.R. Gao, H. Yasuda, M. Kolbe, and G. Wilde: *Scr. Mater.*, 2014, vol. 82, pp. 5–8.
17. D.D. Zuo, J. Chang, W. Liu, and H.P. Wang: *J. Alloy. Compd.*, 2022, vol. 896, 162928.
18. C.Z. Zhang, C.G. Chen, X.H. Liu, M.J. Yan, M. Qi, X.C. Li, Y. Li, H.F. Zhang, F. Yang, W.W. Wang, and Z.M. Guo: *Mater. Sci. Eng. A*, 2022, vol. 855, 143948.
19. A. Zafari and K. Xia: *Addit. Manuf.*, 2021, vol. 47, 102270.
20. A. Bobel, L.G. Hector Jr., L. Casalena, L. Jiang, and A.K. Sachdev: *Mater. Sci. Eng. A*, 2022, vol. 847, 143317.
21. X.J. Sun, J. He, B. Chen, L.L. Zhang, H.X. Jiang, J.Z. Zhao, and H.R. Hao: *J. Mater. Sci. Technol.*, 2020, vol. 44, pp. 201–08.
22. T. Nagase, M. Suzuki, and T. Tanaka: *J. Alloy. Compd.*, 2015, vol. 619, pp. 267–74.
23. B. Zhai, Q. Wang, J. Chang, and H.P. Wang: *Metall. Mater. Trans. B*, 2022, vol. 53B, pp. 2884–96.
24. A.F. Andreoli, O. Shuleshova, V.T. Witusiewicz, Y.H. Wu, Y.Z. Yang, O. Ivashko, A.C. Dippel, M.V. Zimmermann, K. Nielsch, and I. Kaban: *Acta Mater.*, 2021, vol. 212, 116880.
25. W. Liu, B. Zhai, J.F. Zhao, X. Cai, N. Yan, and H.P. Wang: *Metall. Mater. Trans. B*, 2020, vol. 51B, pp. 1784–94.
26. P.C. Zhang, J. Chang, and H.P. Wang: *Metall. Mater. Trans. B*, 2020, vol. 51B, pp. 327–37.
27. H.J. Moon, T.M. Yeo, S.H. Lee, and J.W. Cho: *Scr. Mater.*, 2021, vol. 205, 114218.
28. S.C. Liu, S.P. Yue, J.C. Jie, S.S. Xu, Y. Dong, B.W. Dong, X.Z. Li, and T.J. Li: *J. Alloy. Compd.*, 2023, vol. 938, 168550.
29. S.C. Liu, S.S. Xu, J.C. Jie, J.J. Zhang, Y. Dong, X.Z. Li, and T.J. Li: *J. Alloy. Compd.*, 2021, vol. 888, 161627.
30. Y.B. Jeong, H.R. Jo, J.T. Kim, S.H. Hong, and K.B. Kim: *J. Alloy. Compd.*, 2019, vol. 786, pp. 341–45.
31. D.W. Yuan, H. Zeng, X.P. Xiao, H. Wang, B.J. Han, B.X. Liu, and B. Yang: *Mater. Sci. Eng. A*, 2021, vol. 812, 141064.
32. B.X. Song, T.B. Yu, X.Y. Jiang, W.C. Xi, and X.L. Lin: *J. Mater. Res. Technol.*, 2020, vol. 9, pp. 6464–74.
33. Z.X. Xie, H.Y. Gao, Q. Lu, J. Wang, and B.D. Sun: *J. Alloy. Compd.*, 2010, vol. 508, pp. 320–23.
34. H.Y. Gao, J. Wang, D. Shu, and B.D. Sun: *Scr. Mater.*, 2006, vol. 54, pp. 1931–35.
35. X. Shan and H. Chen: *Phys. Rev. E*, 1994, vol. 49(4), pp. 2941–48.
36. X. Shan and H. Chen: *Phys. Rev. E*, 1993, vol. 47(3), pp. 1815–19.
37. C.J. Smithells: *Smithells Metals Reference Book*, 6th ed. Butterworth, London, 1983.
38. J.F. Xu and B. Wei: *Acta Phys. Sin-Ch. Ed.*, 2005, vol. 54, pp. 3444–50.